An edited version of this paper was published by AGU. Copyright (2019) American Geophysical Union. Nishida, K., T. Maeda, and Y. Fukao. (2019), Seismic observation of tsunami at island broadband stations, *J. Geophys. Res. Solid Earth*, 124. To view the published open abstract, go to https://doi.org/10.1029/2018JB016833

Seismic observation of tsunami at island broadband stations

Kiwamu Nishida[1], Takuto Maeda[2], Yoshio Fukao[3]

[1]Earthquake Research Institute, University of Tokyo, 1-1-1 Yayoi, Bunkyo-ku, Tokyo 113-0032, Japan
[2]Hirosaki University, Hirosaki, Japan
[3]Japan Agency for Marine-Earth Science and Technology, Yokosuka, Japan

Key Points:

- For quantification of seismic observation of tsunami, we evaluate scattering of an incident tsunami for an axisymmetric structure.
- Ground deformation due to the tsunami loading is modeled using static Green's functions.
- By fitting the modeled displacement to observed seismic data, the incident tsunami is inferred from the seismic observation.

Corresponding author: Kiwamu Nishida, knishida@eri.u-tokyo.ac.jp

Abstract

Previous studies have reported seismic observations of tsunami recorded at island broadband stations. Coastal loading by the tsunami can explain them. For further quantification, we model tsunami propagation assuming an axisymmetric structure: a conical island with a flat ocean floor. The total tsunami wavefield can be represented by superposition between an incident tsunami wave and the scattering. The ground deformation due to the total tsunami wavefield at the center is calculated using static Green's functions for elastic half-space with a first-order correction for bathymetry. By fitting the modeled displacement to observed seismic data, we can infer the incident tsunami wave, which can be interpreted as the virtual tsunami amplitude without the conical island. First, we apply this new method to three components of seismic data at a volcano island, Aogashima, for the 2015 Torishima-Oki tsunami earthquake. The estimated tsunami amplitude from the vertical component is consistent with the offshore array observation of absolute pressure gauges close to the island (1.5–20 mHz). The estimated incident azimuth from the three components is also consistent with ray theory. Second, we apply this method to seismic data at four island broadband stations in the Indian ocean for the 2010 Mentawai tsunami earthquake in Indonesia. Despite the limited observed frequency range from 0.5–2.0 mHz, the amplitudes and incident azimuths are consistent with past studies. These observations can complement offshore tsunami observations. Moreover, this method is applicable not only for a tsunami but also for background ocean infragravity wave activity.

1 Introduction

Crustal deformation beneath the ocean due to a massive shallow earthquake generates tsunami (e.g. Satake, 2015). Physically, these are also known as ocean infragravity waves or ocean external gravity waves. Although tsunami amplitudes are usually small in the deep ocean, they increase drastically as tsunami approaches the coast. Such large amplitudes cause severe damage in coastal areas. Understanding tsunami propagation is important for effectively evaluating the risk. Tsunami observations are also crucial for characterizing the source processes of an earthquake (e.g. Satake, Fujii, Harada, & Namegaya, 2013). Observations by offshore ocean bottom pressure gauges (*e.g.* Deep-ocean Assessment and Reporting of Tsunamis (DART) (Bernard & Meinig, 2011)) are typically used for source inversion because of simple wave propagation in the pelagic environment.

Loading on the seafloor by tsunami causes ground deformation of the ground, and vice versa, which is detectable by land-based broadband seismic stations. For example, when the 2010 Maule earthquake hit Chile, a high-density tiltmeter network in Japan recorded ground tilt motions with a typical period of approximately one hour over a broad inland area facing the Pacific coast (Kimura, Tanaka, & Saito, 2013). Simple 2-D modeling for the deformation induced by the Chilean tsunami explained the observed tilt motions in the Japanese island arc (Kimura et al., 2013). During the 2004 Sumatra–Andaman earthquake, tilt motions from 0.3–0.6 mHz were recorded by a broadband seismometer at Showa station at the mouth of a bay in Antarctica (Nawa et al., 2007), and tilt motions with typical periods of approximately 1000 s were recorded by broadband seismometers at stations on islands in the Indian ocean (Yuan, Kind, & Pedersen, 2005). Although the order of observed amplitudes can be explained by tilt motions caused by tsunami loading, the mechanism is not yet fully understood.

Figure 1 shows an example of broadband seismic records at a volcano island, Aogashima, associated with tsunami when the 2015 Torishima earthquake (see section 5 for details). The observed larger amplitudes in horizontal components suggest the effect of tilt motions is dominant. All the seismic records lack the higher-frequency content.

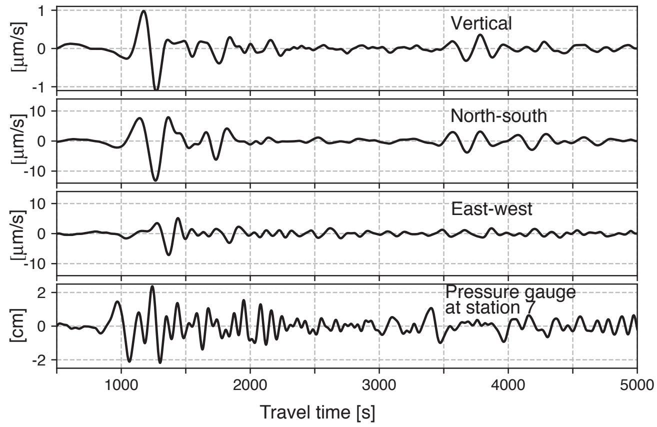

Figure 1. The upper three records show 3 components of the ground velocity recorded by a broadband seismometer at Aogashima (N.AOGF). The lowest record shows tsunami height at an offshore pressure gauge (station 7 shown in Figure 2). All the records are bandpass-filtered from 2 to 20 mHz.

To quantify ground motions at islands, we model the sloping effects in a semi-analytic manner for an axisymmetric conical island with a flat ocean floor (Fujima & Goto, 1994; Kânoğlu & Synolakis, 1998; Smith & Sprinks, 1975). Although the model is simple, it can express the complex wave propagation close to the shoreline. This simple model can explain the spatial pattern of coastal tsunami amplification around islands.

In section 2, we present a theory of tsunami propagation when an arbitrary tsunami wavefield enters a conical island. In section 3, we then estimate the ground deformation at the center of the island due to tsunami loading, which can be related to the incident tsunami wavefield. In section 4, using the axisymmetric assumption, we propose a new technique for estimating virtual tsunami amplitude without a conical island, which could be a proxy for offshore tsunami amplitude. In section 5, this method is applied to two examples: the 2015 Torishima earthquake in Japan and the 2010 Mentawai tsunami earthquake in Indonesia.

2 Theory of tsunami propagation for a conical island with a flat ocean floor

In this study, we consider scattering of tsunami around an axisymmetric conical island. For simplicity, we assume that the tsunami can be approximated as a linear long-wave because dispersion effects should be less important than topographic effects in this case. Following (Gill, 1982), we consider shallow-water equations derived using the hydrostatic approximation. The displacement amplitude of the sea surface disturbance $\eta(r, \theta; t)$ satisfies the following governing equation in time domain:

$$\frac{\partial^2 \eta(r, \theta; t)}{\partial t^2} = g_0 \nabla_h \left[D(r) \nabla_h \eta(r, \theta; \omega) \right], \tag{1}$$

where r is the radius, θ is the azimuth (Figure 3), g_0 is the gravity constant, ∇_h represents the spatial gradient in 2-D, and $D(r)$ is an axisymmetric water depth given

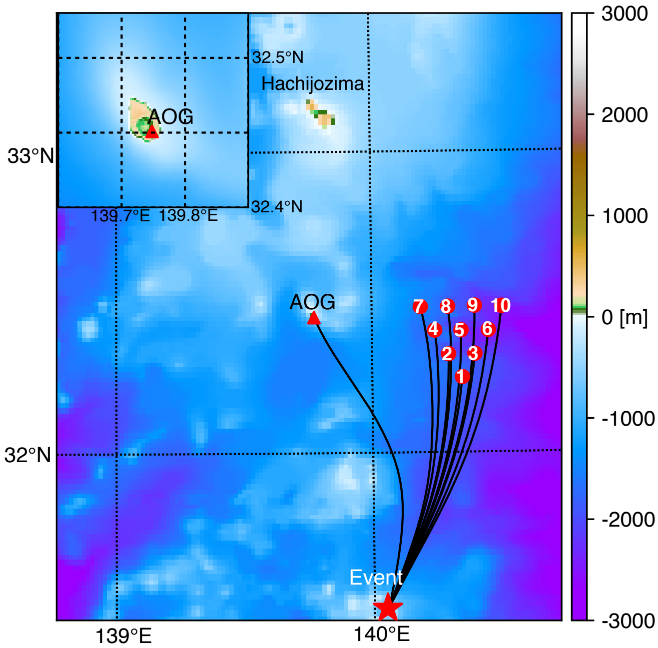

Figure 2. Station distribution of an array of 10 offshore pressure gauges (circles). The inset shows an enlarged map of Aogashima (AOG). The star symbol shows the hypocenter of the earthquake near Torishima on May 2, 2015. At approximately 33.1°N, Hachijojima north to Aogashima is also shown. The station numbers are shown in red circles.

by

$$D(r) = \begin{cases} 0 & \text{if } r < r_0, \\ m(r - r_0) & \text{if } r_0 \le r < r_1, \\ D_0 & \text{if } r_1 \le r, \end{cases} \tag{2}$$

where r_1 is the radius of the root of the island, r_0 is the radius of the island, D_0 is the sea surface height of the flat ocean from the sea bottom, and m is the slope given by $D_0/(r_1 - r_0)$. The frequency-domain representation $\eta(r, \theta; \omega)$ satisfies the following equation:

$$-\omega^2 \eta(r, \theta; \omega) = g_0 D(r) \nabla_h^2 \eta(r, \theta; \omega) + g_0 \nabla_h D(r) \cdot \nabla_h \eta(r, \theta; \omega), \tag{3}$$

where ω is the angular frequency.

We note that, for negative frequency, $\eta(r, \theta, -\omega)$ is defined as the complex conjugate by $\eta^*(r, \theta; \omega)$ because the time domain representation should be a real function. A Fourier component at a negative frequency $-\omega$ is, thus, defined by the complex conjugate of that at a positive frequency ω. Here, we use the Fourier convention:

$$F(\omega) = \int_{-\infty}^{\infty} f(t) e^{-i\omega t} dt, \tag{4}$$

where f is an arbitrary function as a function of time, t, and F is its Fourier component.

At high frequency, tsunami velocity $\sqrt{g_0 D(r)}$ near the coast decreases towards zero. The coastal low-velocity region traps tsunami energy, which enhances tsunami run-up height (e.g. Liu, Cho, Briggs, Lu, & Synolakis, 1995; Satake, 2015). Zero velocity at the coast makes the governing equation singular. By using the axisymmetric approximation, however, an analytic evaluation of the singularity becomes possible (Fujima & Goto, 1994).

Because the governing equation is axisymmetric, tsunami wavefield $\eta(r,\theta;\omega)$ can be expanded by a Fourier series with respect to the azimuth, in general, as:

$$\eta(r,\theta;\omega) = \frac{1}{2}\phi_0(r;\omega) + \sum_{n=1}^{\infty}\left[\phi_n(r;\omega)\cos(n\theta) + \phi_{-n}(r;\omega)\sin(n\theta)\right], \quad (5)$$

where $\phi_n(r;\omega)$ is the radial function of azimuthal order n. We assume that an arbitrary incident tsunami wave $\eta^{in}(r,\theta;\omega)$ enters the island and is scattered in the sloping bottom (region II in Figure 3); thus, the total wavefield $\eta(r,\theta;\omega)$ in the flat ocean (region I in Figure 3) can be represented by superposition between the incident wave and the scattered wave (Fujima & Goto, 1994; Kânoğlu & Synolakis, 1998; Smith & Sprinks, 1975). In the following subsections, we evaluate $\phi_n(r;\omega)$ by considering the scattering for an arbitrary incident wave field using a semi-analytic method (Fujima & Goto, 1994; Kânoğlu & Synolakis, 1998).

2.1 Incident tsunami wavefield

First, let us consider an arbitrary incident arbitrary wavefield $\eta^{in}(r,\theta;\omega)$ in a flat ocean without the conical island virtually. The incident wavefield in a flat ocean η^{in} can be expanded by a Fourier series with respect to the azimuth and Bessel functions of the first kind with respect to the radial direction as follows:

$$\eta^{in}(r,\theta;\omega) = \frac{1}{2}\zeta_0^{in}(\omega)J_0(k_0 r) + \sum_{n=1}^{\infty}\left[\zeta_n^{in}(\omega)\cos(n\theta) + \zeta_{-n}^{in}(\omega)\sin(n\theta)\right]J_n(k_0 r), \quad (6)$$

where J_n is the nth order Bessel function of the first kind, k_0 is the wavenumber given by $\omega/\sqrt{g_0 D_0}$, and $\zeta_n^{in}(\omega)$ is the coefficient.

2.2 Wave scattering by a conical island in a flat ocean (I)

The incident wave $\eta^{in}(r,\theta;\omega)$ enters the conical island area and the scattered wave amplitude is represented by $\eta^{sc}(r,\theta;\omega)$. The total tsunami amplitude η can be written as

$$\eta(r,\theta;\omega) = \eta^{in}(r,\theta;\omega) + \eta^{sc}(r,\theta;\omega). \quad (7)$$

Let us consider the scattered wavefield $\eta^{sc}(r,\theta;\omega)$ for the flat ocean floor (I) (see Figure 3). The scattered wavefield $\eta^{sc}(r,\theta;\omega)$ can be represented by an outgoing wave in the flat ocean according to the causality of the scattered wave. For a positive angular frequency ω, the scattered wavefield can be written as

$$\eta^{sc}(r,\theta;\omega) = \frac{1}{2}B_0(\omega)\zeta_0^{in}(\omega)H_0^{(2)}(k_0 r) + \sum_{n=1}^{\infty}\left[B_n(\omega)\zeta_n^{in}(\omega)\cos(n\theta) + B_{-n}(\omega)\zeta_{-n}^{in}(\omega)\sin(n\theta)\right]H_n^{(2)}(k_0 r), \quad (8)$$

where $H_n^{(2)}(\omega)$ is the nth order Hankel function of the second kind, which represents outgoing waves, and B_n shows the relative amplitudes of the scattered wave.

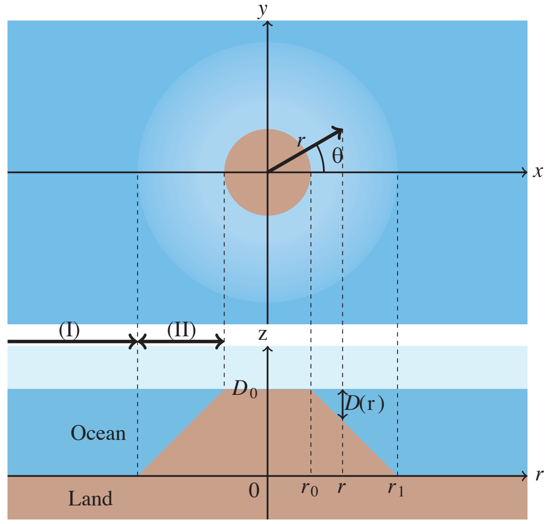

Figure 3. Schematic figure of the conical island. The upper panel shows the plan view of the island, and the lower panel shows the cross-section. The radius on the surface is r_0 and that of the base is r_1.

In summary, $\phi_n(r;\omega)$ (equation (5)) in this region (I) is given by

$$\phi_n(r;\omega) = \left(B_n(\omega)H_n^{(2)}(k_0(\omega)r) + J_n(k_0(\omega)r)\right)\zeta_n^{in}(\omega). \tag{9}$$

We note that the Bessel functions represent the incident waves and the Hankel functions represent the outgoing scattered waves.

2.3 Tsunami wavefield above the sloping bottom in region (II)

For the numerical calculation of $\phi_n(r;\omega)$ within region (II) ($r_0 \leq r \leq r_1$), we define the amplitude A_n and the normalized radial function R_n as:

$$\phi_n(r;\omega) = A_n(\omega)R_n(r;\omega)\zeta_n^{in}(\omega), \tag{10}$$

where R_n is normalized so that $R_n(r_0;\omega) = 1$ and A_n is the amplitude factor of ϕ_n at $r = r_0$. Equation (5) in region (II) can be rewritten as follows:

$$\begin{aligned}\eta(r,\theta;\omega) = {} & \frac{1}{2}A_0(\omega)\zeta_0^{in}(\omega)R_0(r;\omega) \\ & + \sum_{n=1}^{\infty}\left[A_n(\omega)\zeta_n^{in}(\omega)\cos(n\theta) + A_{-n}(\omega)\zeta_{-n}^{in}(\omega)\sin(n\theta)\right]R_n(r;\omega).\end{aligned} \tag{11}$$

Inserting $\eta(r,\theta;\omega)$ into the governing equation (equation (3)) leads to the following equation of R_n:

$$\frac{d^2R_n(r;\omega)}{dr^2} + \left(\frac{1}{r} + \frac{1}{D(r)}\frac{dD(r)}{dr}\right)\frac{dR(r;\omega)}{dr} + \left(\frac{\omega^2}{g_0D(r)} - \frac{n^2}{r^2}\right)R_n(r;\omega) = 0. \tag{12}$$

Following Fujima and Goto (1994), we define the following dimensionless parameters, ξ and β, to characterize this system. $\xi(r)$ is the radial phase defined as

$$\xi(r) \equiv \int_{r_0}^{r} k(r')dr' = 2\omega\sqrt{\frac{(r-r_0)}{g_0}} \quad \text{if } r_0 \leq r \leq r_1, \tag{13}$$

where $k(r)$ is the local wave number given by

$$k(r) \equiv \frac{\omega}{\sqrt{g_0 D(r)}}. \tag{14}$$

β is the azimuthal number along a circle with a radius of $2r_0$ defined by

$$\beta \equiv \left.\frac{2\pi r}{\lambda(r)}\right|_{r=2r_0}, \tag{15}$$

where $\lambda(r)$ is wavelength defined by $2\pi/k(r)$. The reason for choosing this radius is discussed in section 6.

The change of variables from r and h to ξ and β leads to the following equation:

$$\frac{d^2R_n(\xi;\omega)}{d\xi^2} + \left(\frac{2\xi}{\xi^2+\beta^2} + \frac{1}{\xi}\right)\frac{dR_n(\xi;\omega)}{d\xi} + \left(1 - \left(\frac{2\xi}{\xi^2+\beta^2}\right)^2 n^2\right)R_n(\xi;\omega) = 0. \tag{16}$$

Only in two extreme cases of the radius of the island ($r_0 = 0$ and $r_0 = \infty$) (Fujima & Goto, 1994) can we obtain the analytical solutions of $R(\xi)$, which are crucial for understanding the behavior of $R(\xi)$. Two independent solutions exist according to the governing equation; the only one satisfies the physical requirement, which is a finite amplitude of η at the shoreline. First, let us consider the analytical solution for an infinite radius of the island, which also represents a flat sloping bottom. Because β becomes infinite, $R_n(\xi)$ is given by

$$R_n(\xi) \sim J_0(\xi). \tag{17}$$

Next, let us consider the analytical solution for the zero island radius case $r_0 = 0$. Because β becomes 0, $R_n(\xi)$ can be given by

$$R(\xi) \sim \frac{J_{\sqrt{1+4n^2}}(\xi)}{\xi}. \tag{18}$$

Here, we choose a solution that has a finite amplitude at $\xi = 0$. At $\xi = 0$, only $R_0(\xi)$ has a non-zero value, whereas $R_n(0) = 0$ for $n \neq 0$. In general, $R_n(\xi)$ has a significant value at $\xi = 0$ when $n \leq \beta$ (Fujima & Goto, 1994). Since the evaluation of the ground deformations requires only R_n for $n = 0, \pm 1$, as discussed in the following sections, all the $R_n(\xi)$ have significant values at around $\xi = 0$

This ordinary differential equation can be solved using the numerical Livermore Solver for Ordinary Differential Equations (LSODE) (Radhakrishnan & Hindmarsh, 1993). Although R_n is integrated from $\xi = 0$ outward with respect to ξ, the governing equation at $\xi = 0$ is a singularity. For this reason, $R_n(\xi)$ is integrated from $\xi = \Delta\xi$ numerically. $R_n(\Delta\xi)$ can be evaluated analytically by the asymptote (Fujima & Goto, 1994). $R_n(\Delta\xi)$ can be represented by Taylor expansion up to the second order when $\Delta\xi \ll 1$ and $\beta \neq 0$ (Fujima & Goto, 1994):

$$R_n(\Delta\xi) \approx \left(1 - \frac{1}{4}\Delta\xi^2\right). \tag{19}$$

Accordingly, the first order initial boundary conditions of R_n at $\xi = \Delta\xi$ are given by

$$R_n(\Delta\xi) = 1, \tag{20}$$

$$\left.\frac{dR_n(\xi)}{d\xi}\right|_{\xi=\Delta\xi} = -\frac{1}{2}\Delta\xi. \tag{21}$$

2.4 Boundary condition between (I) and (II)

We evaluate the boundary condition between (I) and (II) at $r = r_1$ for this equation. Continuity of the amplitude for each azimuthal order, n, and the first derivative at the boundary between regions (I) and (II) leads to the following boundary condition:

$$A_n(\omega)R_n(\xi_1) = J_n(k_0r_1) + B_n(\omega)H_n^{(2)}(k_0r_1), \tag{22}$$

$$A_n(\omega)\left.\left(\frac{dR_n(\xi)}{d\xi}\frac{d\xi}{dr}\right)\right|_{\xi=\xi_1} = \left.\frac{dJ_n(k_0r)}{dr}\right|_{r=r_1} + B_n(\omega)\left.\frac{dH_n^{(2)}(k_0r)}{dr}\right|_{r=r_1}, \tag{23}$$

where $\xi_1 \equiv \xi(r_1)$. We can estimate A_n and B_n by solving this equation.

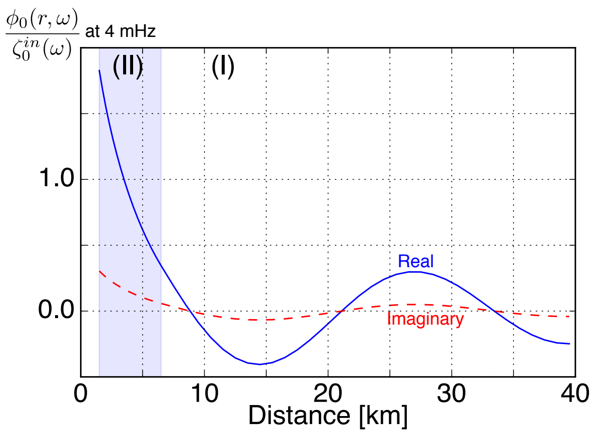

Figure 4. $\phi_0(r;\omega)/\zeta_0(\omega)$ at 4 mHz for Aogashima, the parameters of which are given in Table 1. The blue line shows the real part and the red dashed line shows the imaginary part.

Figure 4 shows the induced tsunami wavefield with azimuthal order 0 for the unit amplitude of the incident wave ($\phi_0(r,\omega)/\zeta_0^{in}(\omega)$) at 4 mHz. The parameters are those for Aogashima given in Table 1. At approximately $r = r_0$, $\phi_0(r;\omega)/\zeta_0^{in}(r;\omega)$ is larger than 1, which indicates amplification due to confinement along the coast. We discuss this in detail in section 6.

3 Ground deformation by tsunami loading

To estimate ground motions due to tsunami, we assume that they can be represented by static deformation caused by tsunami loading (e.g. Sorrells & Goforth, 1973) because the phase velocity of seismic waves (on the order of 4 km/s) is much faster than that of a tsunami (on the order of 0.01 km/s) in coastal areas. Loading on the seafloor by the modeled tsunami wavefield is convolved with static Green's functions in a semi-infinite medium with the following correction for bathymetric effects. Because the radius of the island, r_0, is much smaller than r_1 in most cases, we evaluate the deformation, $\boldsymbol{u}(\omega)$, at the center of the island for simplicity. Note that the tilt mo-

Table 1. Parameters (radius of the island r_0, slope m, and ocean depth D_0) used in this study based on ETOPO1 (Amante & Eakins, 2009). These parameters were estimated by the non-linear least-squares technique using MINPACK (Moré et al., 1984) with trial and error. f_β is a reference frequency used as $\beta = 1$ in equation (15).

station	radius r_0 [km]	slope m	ocean depth D_0 [km]	f_β [mHz]
AOG	1.5	0.20	1.0	2.9
RER	29	0.070	4.2	0.39
AIS	4.9	0.18	2.0	1.5
DGAR	12	0.017	4.2	0.29
CRZF	10	0.034	3.0	0.45

tion at the center is also calculated because the horizontal component of a broadband seismometer is sensitive to tilt motion in this frequency range (Aki & Richards, 1980).

To evaluate the bathymetric correction for the Green's functions in a semi-infinite medium, the displacement $\boldsymbol{u}(x, y, z)$ and stress $\boldsymbol{\sigma}(x, y, z)$ in a Cartesian coordinate system (x, y, z) is expanded by the powers of slope, m, up to the first order (Segall, 2010; Williams & Wadge, 2000):

$$u_i(x, y, z; \omega) = u_i^{(0)}(x, y, z; \omega) + u_i^{(1)}(x, y, z; \omega)m + \mathcal{O}(m^2), \qquad i = x, y, z \tag{24}$$

$$\sigma_{ij}(x, y; \omega) = \sigma_{ij}^{(0)}(x, y, z; \omega) + \sigma_{ij}^{(1)}(x, y, z; \omega)m + \mathcal{O}(m^2), \qquad i, j = x, y, z, \tag{25}$$

where $\mathcal{O}$ indicates "order of", u_i is the displacement, σ_{ij} is the stress, $^{(0)}$ shows the 0th order term, and $^{(1)}$ shows the first order terms. Based on the estimation of the first order terms described in appendix A, the first order terms with respect to the slope, m, becomes comparable to the second order terms. Therefore, we neglect the first order terms below.

The displacement and tilt on the surface ($z = D_0$) and at the center ($x = y = 0$) are corrected for elevation from $z = 0$ as follows:

$$u_\alpha(0, 0, D_0) = u_\alpha^{(0)}(0, 0, 0) - D_0 \left.\frac{\partial u_z^{(0)}}{\partial \alpha}\right|_{z=0}, \qquad \alpha = x, y, \tag{26}$$

$$u_z(0, 0, D_0) = u_z^{(0)}(0, 0, 0), \tag{27}$$

$$\left.\frac{\partial u_z}{\partial \alpha}\right|_{x=y=0, z=D_0} = \left.\frac{\partial u_z^{(0)}}{\partial \alpha}\right|_{x=y=z=0}, \qquad \alpha = x, y. \tag{28}$$

The first-order corrections of horizontal displacement according to the location change are related to the corresponding 0th-order tilt motions. The correction of vertical displacement and tilt motion according to the location change is negligible in the first order because the surface pressure causes a vertical strain $\partial u_z^{(0)}/\partial z = 0$ at the free surface in a half space (Farrell, 1972).

Static Green's functions $g_r^z(r)$, $g_\theta^z(r)$, and $g_z^z(r)$ at a surface point $\boldsymbol{r} = (r, \theta, 0)$ for a vertical force at the origin in a semi-infinite medium are given by (Jaeger, Cook,

& Zimmerman, 2007; Segall, 2010)

$$g_r^z(r) = \frac{1}{4\pi}\frac{1}{\lambda+\mu}\frac{1}{r}, \tag{29}$$

$$g_\theta^z(r) = 0, \tag{30}$$

$$g_z^z(r) = \frac{1}{4\pi\mu}\frac{\lambda+2\mu}{\lambda+\mu}\frac{1}{r}, \tag{31}$$

where r is the radius in a cylindrical coordinate system (Figure 3), μ, and λ are Lamé's constant of the ground, the superscript on the Green's tensors refers to the direction of the point force, and the subscript refers to the direction of displacement. By convolving forcing by the total tsunami wavefield and the static Green's functions with bathymetric corrections, we can estimate the displacement and tilt at the center.

4 Virtual tsunami amplitude and direction without a conical island

Based on the total tsunami wavefield (section 2) and the Green's functions (section 3), we can relate the ground particle velocity at the center to the incident tsunami using a transfer function. The axisymmetric assumption of the island simplifies the transfer function concerning the azimuthal dependence. By deconvolving the transfer function from observed seismic data in the vertical component, we can infer the incident tsunami amplitude, η^v, at the center assuming that the island is virtually removed. By deconvolving the transfer function from observed seismic data in the horizontal component, we can estimate the spatial gradient of η^v, which shows the propagation direction together with a single plane wave assumption.

4.1 Transfer function of the vertical component

The vertical ground velocity at the origin $v_z(\omega)$ due to the tsunami deformation can be represented by convolution between tsunami loading and the static Green's function as:

$$v_z(\omega) = -\rho g_0 \omega e^{i\pi/2}\int_{r_0}^{\infty}\int_0^{2\pi}\eta(r,\theta;\omega)g_z^z(r)rdrd\theta, \tag{32}$$

where $v_z(\omega)$ is the particle velocity in the z component given by $i\omega u_z(\omega)$. Let us evaluate the integration using equations (5), (9), and (10). Because the integrand is axisymmetric, the higher order contributions with respect to azimuthal order ($n \geq 1$) such as:

$$-\rho g_0 \omega e^{i\pi/2}\int_{r_0}^{\infty}\phi(r;\omega)g_z^z(r)rdr\int_0^{2\pi}\cos(n\theta)d\theta \tag{33}$$

are canceled out. Here, we define the virtual tsunami amplitude, $\eta^v(\omega)$, without the island as

$$\eta^v(\omega) \equiv \eta^{in}(r,\theta;\omega)\big|_{r=0}. \tag{34}$$

The virtual tsunami amplitude can be related to the particle velocity v_z using a transfer function $T_{\eta z}$:

$$v_z(\omega) = T_{\eta z}(\omega)\eta^v(\omega), \tag{35}$$

where $T_{\eta z}(\omega)$ is the transfer function of the tsunami to vertical ground velocity, defined as

$$T_{\eta z}(\omega) \equiv -e^{i\pi/2}\pi\omega\rho g_0\left(I_1^z(\omega)+I_2^z(\omega)\right), \tag{36}$$

The integrals I_1^z and I_2^z are defined as

$$I_1^z(\omega) \equiv \int_{r_1}^{\infty} \left(B_0(\omega) H_0^{(2)}(k_0 r) + J_0(k_0 r) \right) g_z^z(r) r dr, \tag{37}$$

$$I_2^z(\omega) \equiv \int_{r_0}^{r_1} A_0(\omega) R_0(r) g_z^z(r) r dr, \tag{38}$$

respectively. Figure 5a shows an example of the vertical transfer function $T_{\eta z}(\omega)$ for Aogashima. Below 5 mHz, the transfer function is flat. At 0 frequency, the amplitude and phase of the transfer function can be explained by the theoretical solution for a flat ocean (Ben-Menahem & Singh, 2000) as discussed in section 6. The amplitude decreases with a frequency above 5 mHz because tsunami wavelength becomes smaller than the island scale r_0.

4.2 Transfer function of the horizontal component

Let us consider the transfer function of the horizontal component for tsunami incidence in the same manner. The horizontal ground velocity at the origin $\boldsymbol{v}_h(\omega)$ due to tsunami deformation can be represented by

$$\boldsymbol{v}_h(\omega) \equiv \begin{pmatrix} v_x(\omega) \\ v_y(\omega) \end{pmatrix} = -\rho g_0 \omega e^{i\pi/2} \int_{r_0}^{\infty} \int_0^{2\pi} \eta(r, \theta; \omega) \left(g_r^z - D_0 \frac{\partial g_z^z}{\partial r} \right) \begin{pmatrix} -\cos\theta \\ -\sin\theta \end{pmatrix} r dr d\theta. \tag{39}$$

Because $\cos\theta$ and $\sin\theta$ have orthogonality with respect to the azimuthal integration, only $n = \pm 1$ in terms of η contributes to the integration, as follows:

$$\begin{pmatrix} v_x(\omega) \\ v_y(\omega) \end{pmatrix} = \frac{i}{2} T_{\eta h}(\omega) \begin{pmatrix} \zeta_1^{in} \\ \zeta_{-1}^{in} \end{pmatrix} = i \frac{T_{\eta h}(\omega)}{k_0} \nabla_h \eta^{in}(r, \theta; \omega)\big|_{r=0}. \tag{40}$$

Here, $T_{\eta h}(\omega)$ is given by,

$$T_{\eta h}(\omega) = 2\pi\omega\rho g_0 \left(I_1^h(\omega) + I_2^h(\omega) \right), \tag{41}$$

where integrals I_1^h and I_2^h are defined as

$$I_1^h(\omega) \equiv \int_{r_1}^{\infty} \left(B_1(\omega) H_1^{(2)}(k_0 r) + J_1(k_0 r) \right) \left(g_r^z - D_0 \frac{\partial g_z^z}{\partial r} \right) r dr, \tag{42}$$

$$I_2^h(\omega) \equiv \int_{r_0}^{r_1} A_1(\omega) R_1(r) \left(g_r^z - D_0 \frac{\partial g_z^z}{\partial r} \right) r dr. \tag{43}$$

The spatial gradient of the surface displacement $\nabla_h \eta|_{r=0}$ can be related to the flow rate, $\boldsymbol{Q}$ (Satake, 2015), at the origin defined as

$$\boldsymbol{Q} = \int_{D_0 - D(r)}^{D_0} \boldsymbol{v}_h dz = \frac{i g_0}{\omega} \nabla_h \eta^{in}\big|_{r=0} \tag{44}$$

$D(r)$ is water depth at r and D_0 is water depth of the flat ocean floor (Figure 3).

For simplicity, we assume that η can be represented by a single plane wave incidence with the relative travel time, $\mathcal{T}(r, \theta)$, to the origin. The gradient can be written as

$$\nabla_h \eta^{in}(r, \theta; \omega) = -i\omega \eta^{in}(0, \theta; \omega) \nabla_h \mathcal{T}(r, \theta) = \eta^{in}(0, \theta; \omega)(-i k_0) \boldsymbol{e}_r, \tag{45}$$

where $\boldsymbol{e}_r$ is the propagation direction of the tsunami. Then, we obtain the following relationship:

$$\boldsymbol{v}_h(\omega) = T_{\eta h}(\omega) \eta^v(\omega) \boldsymbol{e}_r. \tag{46}$$

$T_{\eta h}$ represents the transfer function from the tsunami incidence to horizontal ground velocity at the center. This result shows that the observed ground velocity is parallel to the tsunami propagation direction under the single plane-wave assumption. Figure 5a shows an example of the horizontal transfer function $T_{\eta z}(\omega)$ for Aogashima. The transfer function has a broad peak at 5 mHz. At 0 frequency, the amplitude and phase of the transfer function can be explained by the theoretical solution for a flat ocean (Ben-Menahem & Singh, 2000) as discussed in section 6. The amplitude also decreases with a frequency above 5 mHz.

Below 1 mHz, tilt motion induced by tsunami is dominant in the horizontal component of seismic sensors (Kimura et al., 2013; Nawa et al., 2007). The horizontal acceleration contribution due to tilt motion ($\nabla_h u_z$, where u_z is the vertical displacement) is given by $g_0 \nabla_h u_z$ (e.g. Rodgers, 1968; Wielandt & Forbriger, 1999). Then, the tilt motion at the origin, $v(\omega)$, due to deformation by the tsunami can be represented by

$$\boldsymbol{v}_h^{tilt}(\omega) = \frac{g_0 \nabla_h u_z}{i\omega} = \frac{-\rho g_0}{i\omega} \int_{r_0}^{\infty} \int_0^{2\pi} \eta(r,\theta;\omega) \frac{\partial g_r^z}{\partial r} \begin{pmatrix} -\cos\theta \\ -\sin\theta \end{pmatrix} r dr d\theta. \tag{47}$$

The higher order contributions ($n \neq \pm 1$) are again canceled out.

$$\boldsymbol{v}^{tilt}(\omega) = \frac{i}{2} T_{\eta h}(\omega) \begin{pmatrix} \zeta_1^{in} \\ \zeta_{-1}^{in} \end{pmatrix} = i \frac{T_{\eta h}^{tilt}(\omega)}{k_0} \nabla_h \eta^{in}(r,\theta;\omega)\big|_{r=0}. \tag{48}$$

Here, the transfer function due to tilt, $T_{\eta h}^{tilt}(\omega)$, of the tsunami to horizontal ground velocity is given by,

$$T_{\eta h}^{tilt}(\omega) = \frac{2\pi\rho g_0}{\omega} \left(I_1^t(\omega) + I_2^t(\omega) \right), \tag{49}$$

where integrals I_1^t and I_2^t are defined by

$$I_1^t(\omega) \equiv \int_{r_1}^{\infty} \left(B_1(\omega) H_1^{(2)}(k_0 r) + J_1(k_0 r) \right) \frac{\partial g_h^r(r)}{\partial r} r dr, \tag{50}$$

$$I_2^t(\omega) \equiv \int_{r_0}^{r_1} A_1(\omega) R_1(r) \frac{\partial g_z^z(r)}{\partial r} r dr. \tag{51}$$

Then, we also obtain the following relationship:

$$\boldsymbol{v}_h^{tilt}(\omega) = T_{\eta h}^{tilt}(\omega) \eta^v(\omega) \boldsymbol{e}_r. \tag{52}$$

Figure 5b shows that the tilt effects of the horizontal transfer function are dominant, specifically at low frequencies. Below 1 mHz, the transfer function approaches the theoretical solution for a flat ocean (Ben-Menahem & Singh, 2000), which is proportional to ω^{-1}. With increasing frequency, the contribution of the tilt effect decreases. Although the amplitudes of horizontal components are an order of magnitude larger than those of vertical components, the estimated virtual tsunami amplitude from horizontal components is more ambiguous. This is because tilt motions, which are the spatial derivative of vertical motion, are more sensitive to small-scale bathymetric changes and crustal heterogeneity.

5 Comparison with observations

During huge shallow earthquakes, the horizontal components of broadband seismometers located on an island often record tilt motion associated with tsunami (e.g., the 2004 Sumatra earthquake (Yuan et al., 2005)), although the contribution of low-frequency seismic waves excited by the earthquake (Kimura et al., 2013; Yuan et al., 2005) disturbs the tsunami signal. The amplitudes of vertical components are too

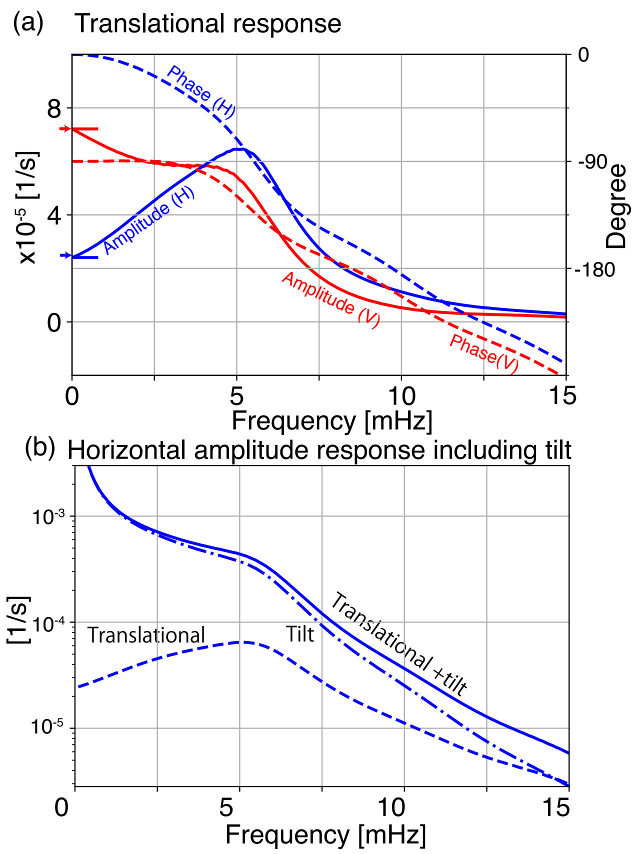

Figure 5. (a) Transfer function of translational motions against frequency. The dashed lines show the phases and the solid lines show the amplitudes, where (V) in the figure represents the vertical component and (H) shows the horizontal component. The red and blue lines show the vertical and horizontal transfer functions, respectively. Red and blue arrows at 0 mHz show theoretical amplitudes for a flat ocean (Ben-Menahem & Singh, 2000) in vertical and horizontal components respectively. The phase shift can be explained by the arrival delay (approximately 70 s). (b) Amplitude of the transfer function of the horizontal component against frequency according to the contribution of translational motion, tilt motion, and both. The contribution of tilt motion is dominant below 5 mHz. We note that phases of the transfer function due to tilt are analytically the same as those of horizontal transfer function at all frequencies.

small to detect because the vertical response is much smaller than the tilt response, as shown in Figure 5.

In order to suppress the noise, we apply this method to tsunami earthquakes, which cause a much larger tsunami than expected from the seismic moment. We determine the virtual tsunami amplitude and direction for two tsunami earthquakes: (1) the 2015 volcanic tsunami earthquake near Torishima, Japan, and (2) the 2010 Mentawai tsunami earthquake in Indonesia. These results are verified by ray theory and other geophysical observations.

5.1 Torishima 2015 Earthquake in Japan

A compensated-linear-vector-dipole (CLVD) type earthquake occurred on May 2, 2015, near Torishima island, Izu–Bonin arc, Japan (Figure 2), generating an abnormally large tsunami (*e.g.* 0.5 m at Hachijozima 180 km north of the epicenter) for the moment magnitude of M_w 5.7, determined by the U.S. Geological Survey. The tsunami was caused by large deformation in a shallow part of a submarine volcanic body (Fukao et al., 2018). A triangular array of ocean bottom pressure (OBP) gauges recorded an off-shore tsunami (Sandanbata et al., 2017). They were deployed 100 km northeast of the epicenter with a station separation of approximately 10 km (Figure 2). All tsunami waveforms with amplitudes of approximately 2 cm are similar to each other (Figure 6). A tsunami earthquake with a surface wave magnitude of Ms 5.6 in the same area occurred on June 13, 1984 (Kanamori, Ekström, Dziewonski, Barker, & Sipkin, 1993; Satake & Kanamori, 1991); their focal mechanisms suggest magma injection with the submarine volcano (Fukao et al., 2018; Kanamori et al., 1993).

At Aogashima island, close to the array, a broadband seismometer (STS2) of F-net (Okada et al., 2004) was deployed by the National Research Institute for Earth Science and Disaster Prevention (NIED). Because seismic waves from tsunami earthquakes were relatively small at a low-frequency of 1.5-20 mHz, the broadband seismometer recorded clear ground motions associated with the tsunami (Figure 1). We can compare the estimated virtual tsunami amplitudes from the seismic observations with near deep ocean bottom pressure gauge.

Using the vertical component of the broadband seismometer, we infer the virtual tsunami amplitude. The modeled parameters of the conical island are given in Table (1). Using the transfer function, $T_{\eta z}(\omega)$, shown by Figure 5a, we estimate the virtual tsunami amplitude $\bar{\eta}^v(\omega)$ by deconvolution:

$$\bar{\eta}^v(\omega) = \frac{T^*_{\eta z}(\omega)}{T^*_{\eta z}(\omega)T_{\eta z}(\omega) + w} v_z(\omega), \tag{53}$$

where w is the water level, which is 5×10^{-3} of the squared amplitude of $T_{\eta z}$ at 5 mHz. The $\bar{\eta}^v$ is converted in time domain. Figure 6 shows the comparison of $\bar{\eta}^v(t)$ with observed tsunami amplitudes by the pressure gauges against the relative travel time. The estimated amplitude of approximately 2.5 cm and the relative travel times are consistent with the offshore observations. The ray theoretical arrival times should coincide with the peak time, but the figure shows slight delays in the peak time, which are attributed to dispersion due to the finite wavelength. This result verifies the feasibility of this method.

Next, let us consider the propagation direction from the observed horizontal components shown in Figure 5b. Using the transfer function, $T_{\eta h}$, for horizontal components, the tsunami amplitude with a propagation direction of $(\bar{\eta}^v_x, \bar{\eta}^v_y)$ can be defined as,

$$\begin{pmatrix} \bar{\eta}^v_x(\omega) \\ \bar{\eta}^v_y(\omega) \end{pmatrix} \equiv \frac{T^*_{\eta h}}{T^*_{\eta h}(\omega)T_{\eta h}(\omega) + w} \begin{pmatrix} v_x(\omega) \\ v_y(\omega) \end{pmatrix}, \tag{54}$$

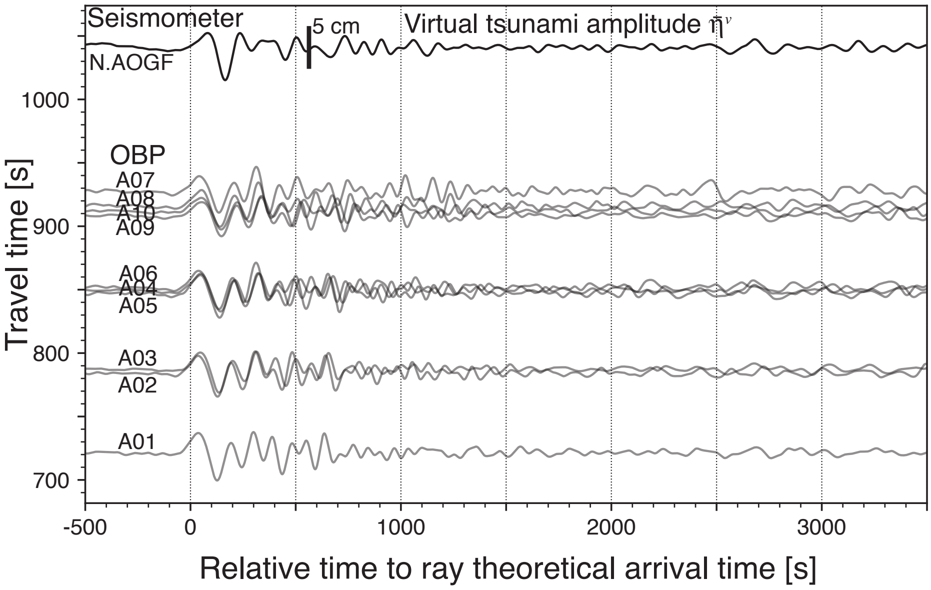

Figure 6. Estimated virtual tsunami amplitude with array observations by absolute pressure gauges. The vertical axis shows travel time predicted by ray theory and the horizontal axis shows relative time to the ray theoretical arrival time. Here, travel times are calculated by fast marching (Rawlinson, 2005; Rawlinson & Sambridge, 2005) using the long wave approximation. The uppermost record shows the virtual tsunami amplitude estimated from the vertical ground velocity at Aogashima (N.AOGF). The lower record shows 10 records of ocean bottom pressure gauges. These records are bandpass filtered from 1.5 to 20 mHz (4th order Butterworth, zero phase). The amplitude scales are the same throughout all records. The maximum amplitudes are approximately 2 cm.

where w is the water level, which is 1×10^{-3} the squared amplitude of $T_{\eta h}$ at 5 mHz. With the single plane wave assumption, $(\bar{\eta}^v_x, \bar{\eta}^v_y)$ can be interpreted as $\eta^{in}\boldsymbol{e}_r$ (equation (46)). Figure 7a shows the comparison among $\bar{\eta}^v_x$, $\bar{\eta}^v_y$, and $\bar{\eta}^v$. The waveforms at approximately 1000 s are consistent with each other.

The particle motions of the horizontal components (Figure 7b) shows a linear polarization, which is consistent with the ray path shown in Figure 2. The consistency suggests that the assumptions related to the approximations of the conical island and the single plane wave are appropriate. Although the horizontal amplitude is slightly larger than the vertical amplitude, the discrepancy can be attributed to the slightly off-center station to the southwest. Phases of the later arrival at approximately 3000 s in Figure 7 are different in different components because they are composed of multiple scattering waves.

To quantitatively estimate the propagation direction, we assume that the virtual tsunami amplitude is given by $\bar{\eta}^v$ from the vertical component. Then, equation (46) leads to

$$\begin{pmatrix} \bar{\eta}^v_x(\omega) \\ \bar{\eta}^v_y(\omega) \end{pmatrix} = \bar{\eta}^v \begin{pmatrix} \sin\varphi \\ \cos\varphi \end{pmatrix}, \tag{55}$$

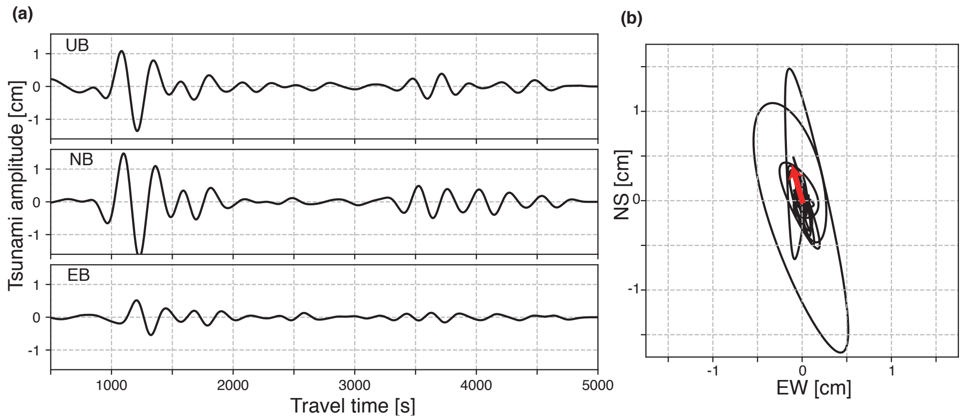

Figure 7. (a) The three components of the estimated tsunami waveform. The first is 2–5 mHz with a 6th order Butterworth filter. (b) Particle motions of the horizontal components from 2 to 5 mHz. The red arrow shows the estimated propagation direction with root mean squared amplitudes from 0 to 500 s.

where φ is the propagation azimuth, which, in this case, can be estimated by

$$\varphi = \frac{\pi}{2} - \arctan 2\left(\int_{t_0}^{t_1} \bar{\eta}_y^v(t)\bar{\eta}^v(t)dt, \int_{t_0}^{t_1} \bar{\eta}_x^v(t)\bar{\eta}^v(t)dt\right), \tag{56}$$

where $\arctan 2$ is 2-argument arc-tangent,t_0 is 0 s, and t_1 is 5000 s. The red arrow in Figure 7 shows the propagation direction φ, whose length shows the root mean squared amplitude from 0 to 5000 s. Because the integration in the above equation, which represents covariance between the vertical and horizontal components, suppress incoherent parts, which originate from the higher noise level and scattered wavefield, the estimation is expected to be robust. Figure 8 shows the comparison between the estimated azimuth and the ray azimuth at the station. This figure shows that they are consistent within 10 degrees. We also note that the above method enables us to estimate the propagation direction without introducing a 180° uncertainty (e.g. Takagi, Nishida, Maeda, & Obara, 2018).

5.2 Mentawai 2010 in Indonesia

The 2010 Mentawai earthquake (Mw 7.8) caused a destructive tsunami in the Mentawai Islands, west of Sumatra in Indonesia (Satake, Nishimura, et al., 2013). The tsunami amplitude reached 9.3 m on the west coasts of North and South Pagai Island. Seismological data analyses show that the earthquake was a tsunami earthquake (e.g. Lay et al., 2011). For the analysis, we use four broadband stations located on islands DGAR, RER, CRZF, and AIS shown in Figure 9. For the estimation of tsunami amplitude, we use the water level (see equations (53) and (54)), which is 5% of the maximum squared amplitude in a frequency range from 0.7 to 2 mHz.

Because most island radii (Table 1) are larger than that of Aogashim, as shown in Figure 10, their transfer functions are not sensitive to tsunami above 1 mHz, as shown in Figure 11. Hence, we focus on a signal with a typical frequency of 1 mHz. The estimated virtual tsunami amplitudes were 0.4 cm at DGAR, 1.3 cm at AIS, 0.9 cm at CRZF, and 0.6 cm at RER. Arrival times of the estimated waveforms are consistent with the ray theoretical values. The arrival time at DGAR is advanced because the simple symmetric model is too simple to model a large island with a larger root size r_1 of approximately 260 km (see Table 1). Although DART station 5601 recorded a

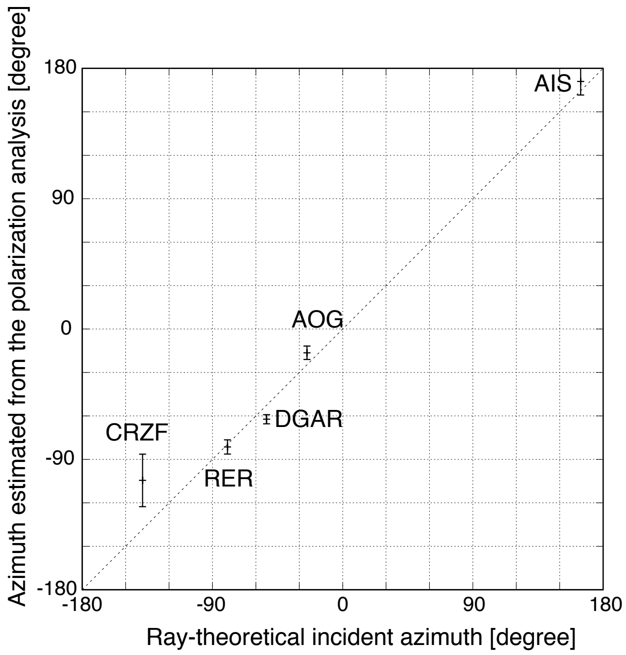

Figure 8. Propagation azimuths at stations. The horizontal axis shows the propagation azimuths estimated by this method utilizing broadband seismic data, whereas the vertical axis shows azimuths based on ray theory. To estimate the error of the propagation azimuth, we made 10^5 bootstrap samples and We estimated the error bars of 1σ by the use of moving block bootstrap resampling (Vogel & Shallcross, 1996). We made 10^5 bootstrap samples with a block length of 50 s at Aogashima and that of 100 s at the other stations respectively.

maximum tsunami amplitude of 1 cm (Satake, Nishimura, et al., 2013), it is located 1,600 km south to the epicenter. Because there are no offshore stations close to the four seismic broadband stations, we compare the virtual tsunami heights $\bar{\eta}^v$ with numerical results by NOAA Center for Tsunami Research, which are maximum tsunami heights at an offshore points close to the stations based on the NOAA forecast method using MOST model with the tsunami source inferred from DART data (Gica, Spillane, Titov, Chamberlin, & Newman, 2008). The calculated maximum wave heights of about 5 mm for RER, about 14 mm for AIS, about 14 mm, and about 8 mm for CRZF are consistent with our estimations.

The map in Figure 9 shows the estimated propagation directions using three components of broadband seismometers, as shown in the previous subsection. Although the estimated azimuths are slightly different from the ray paths on this large scale, the difference can be attributed to strong refraction close to the islands. Indeed, the relationship between the propagation azimuths estimated from the seismic stations can be explained by the azimuths predicted by ray theory, as shown in Figure 8. These are consistent with ray paths within 10 degrees except for CRZF. The deviation could be explained by scattering due to the neighboring island (Figure 10), which may break the single plane wave approximation.

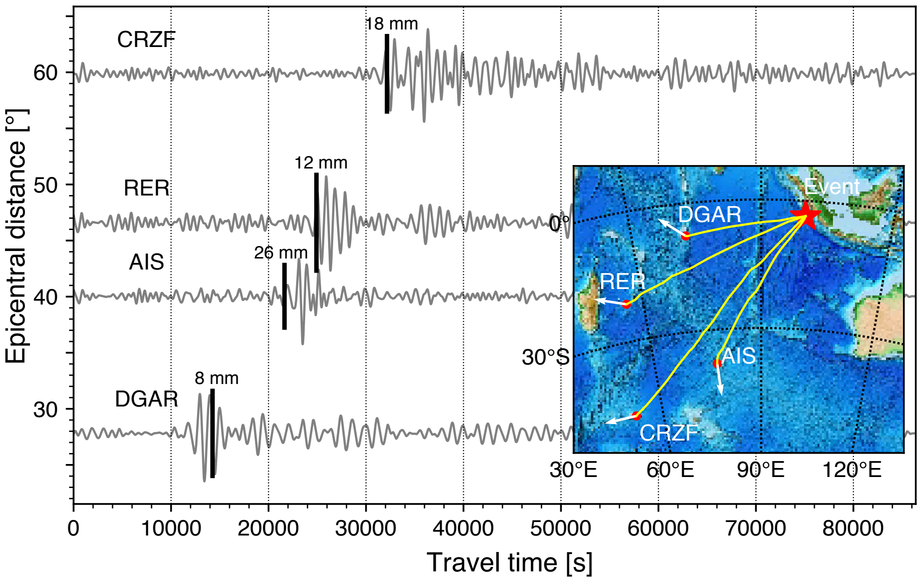

Figure 9. Virtual tsunami amplitudes at four stations for the 2010 Mentawai earthquake (Oct 25, 2010). 0.7–2 mHz (order 6). The map in the inset shows the station locations and the earthquake location. The bold black bars show the corresponding ray theoretical arrival times with amplitude scales.

6 Characteristics of the transfer function according to the slope and radius

Tsunami trapping in the coastal slope of a conical island is crucial for characterizing the transfer functions. This section describes the amplification characteristics due to trapping in coastal areas, where the trapping condition (Longuet-Higgins, 1967) is given by,

$$\frac{\partial}{\partial r}\left(\frac{D(r)}{r^2}\right) \geq 0. \tag{57}$$

For the case of a conical island, the condition can be simplified as

$$r \leq 2r_0. \tag{58}$$

This relationship indicates that a larger conical island will trap more inshore areas.

β defined in equation (15) is crucial for characterizing the trapping effect. β can be interpreted as the ratio of the circumference, $4\pi r_0$ at $r = 2r_0$, to the wavelength, λ. In other words, β shows the azimuthal number of the trapped mode. Here, we define the cut-off frequency f_β as $\beta = 1$. Above this frequency, the tsunami is trapped in inshore areas. f_β is also a good proxy for ground deformation at the center because the deformation becomes significant when the radius of the island becomes larger than the wavelength. Consequently, the ground deformation becomes small with increasing frequency above the frequency. The f_β value, therefore, characterizes the cut-off frequency of the transfer functions. Table 1 shows f_β for the islands, which correspond to the cut-off frequency shown in Figure 11.

With a smaller slope m, more tsunami energy is trapped in the inshore area due to the slow propagation speed. In this case, the transfer function exhibits a peak

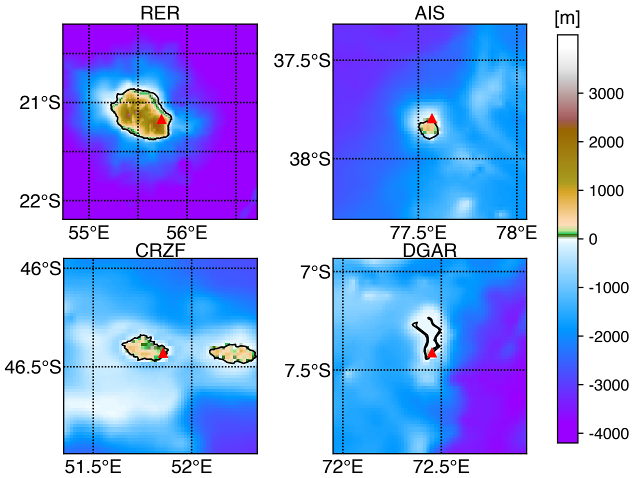

Figure 10. Enlarged maps of the islands. Stations are indicated by red triangles.

at approximately f_β. The translational transfer functions of DGAR and CRZF with smaller slope, m, show peaks at approximately f_β.

At much lower frequencies than f_β, we can neglect scattering by the island because the wavelength of the tsunami becomes much larger than the island scale. Moreover, the contribution of ground deformation in the inshore area becomes negligible. In this limit, the transfer functions are approximated by those of a semi-infinite medium loaded by pressure fluctuations on the surface given by Ben-Menahem and Singh (2000):

$$\lim_{\omega\to 0} T_{\eta z}(\omega) = \frac{e^{-i\pi/2}\sqrt{g_0 D_0}}{2(\lambda+\mu)}\frac{\lambda+2\mu}{\mu}\rho g_0, \tag{59}$$

$$\lim_{\omega\to 0} T_{\eta h}(\omega) = \frac{\sqrt{g_0 D_0}}{2(\lambda+\mu)}\rho g_0, \tag{60}$$

$$\lim_{\omega\to 0} T_{\eta h}^{tilt}(\omega) = \frac{\lambda+2\mu}{2(\lambda+\mu)\mu}\rho\frac{g_0^2}{\omega}. \tag{61}$$

Figure 5a and Figure 11 show that the transfer functions approaching zero frequency also approach the above values. Figure 11 (d) also shows that $T_{\eta h}^{tilt}(\omega)$ actually approaches equation (61) in the low frequency limit.

At frequencies higher than about $10 f_\beta$, the wavelength of tsunami becomes much smaller than the island scale. Consequently, the scattering by small scale bathymetric changes breaks the basic assumption of this method. Thus, f_β could be a proxy for the characteristics when evaluating the transfer function.

7 Potential applications for ocean infragravity waves

Although tsunami in this frequency range is ocean infragravity waves excited by an earthquake, ocean infragravity waves are also excited by the other geophysical processes. For example, they are excited persistently along shorelines by incident ocean swell through nonlinear processes and travel across the ocean with a typical height on the order of 1 cm in pelagic regions (Rawat et al., 2014; Tonegawa et al., 2018). The background ocean infragravity-wave activities are also key for understanding background seismic wavefields know as seismic hum because they are the primary

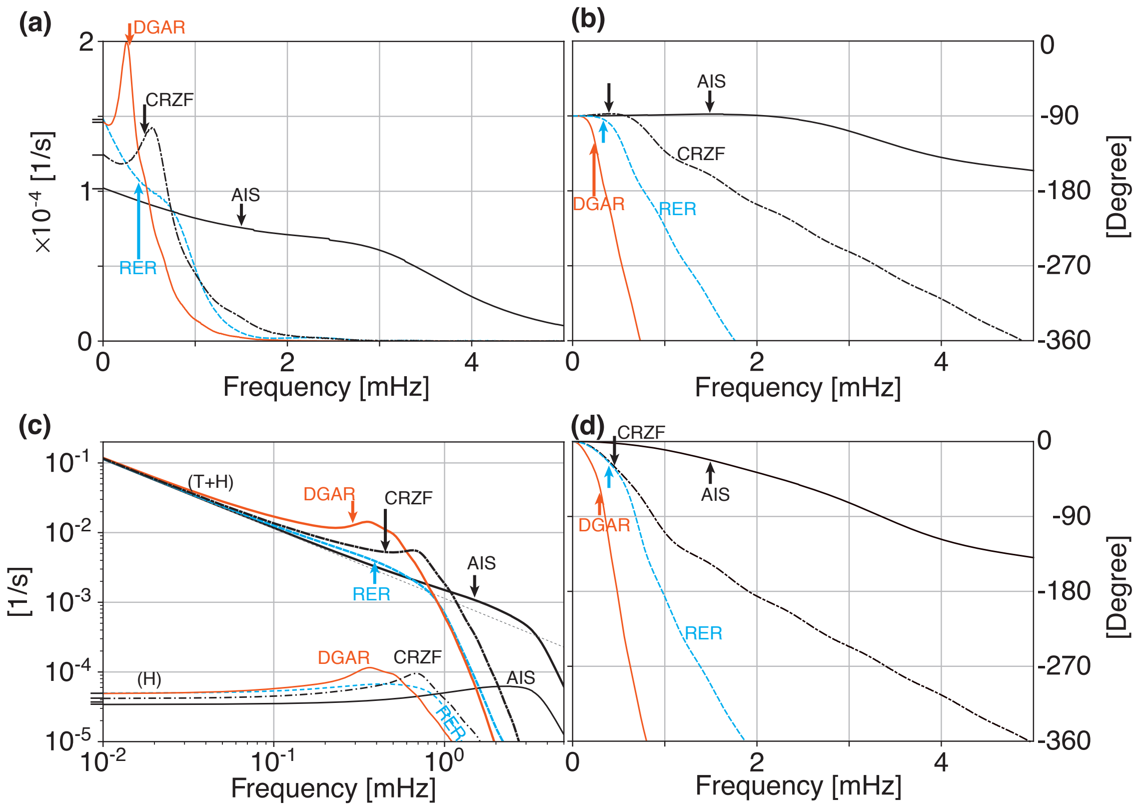

Figure 11. (a) Amplitudes of transfer functions for vertical components against frequency at the four broadband stations, composed of one IRIS IDA station, DGAR (Diego Garcia, Chagos islands), and three GEOSCOPE stations RER (La Réunion Island, France), CRZF (Port Alfred - Ile de la Possession - Crozet Islands, France), and AIS (Nouvel Amsterdam, TAAF, France). Station locations are shown in Figure 9. Black tick marks at 0 mHz show theoretical amplitudes for a flat ocean (equation (59)) in vertical components. The f_β values are shown by arrows. (b) Phases of the transfer functions for vertical components against frequency. (c) Amplitudes of transfer functions for horizontal components against frequency. Labels (H) shows the horizontal components due to translational motion, and (H+T) shows the horizontal component including the tilt effect. Black tick marks at 0 mHz show the theoretical amplitudes for a flat ocean (equation (60)) in horizontal components, and the straight dot-line in gray shows the theoretical amplitudes caused by the tilt motion for a flat ocean (equation (61)). (d) Phases of the transfer functions for horizontal components against frequency.

excitation source (Ardhuin, Gualtieri, & Stutzmann, 2015; Nishida, 2013, 2017; Rhie & Romanowicz, 2004). Observed equipartition of energy between Love and Rayleigh waves (Fukao, Nishida, & Kobayashi, 2010; Nishida, Kawakatsu, Fukao, & Obara, 2008) suggests a topographic coupling between ocean infragravity waves and seismic surface waves. Seismic observations at island broadband stations could be used to understand the excitation mechanisms because modeling of ocean infragravity waves requires further researches (Ardhuin et al., 2015; Ardhuin, Rawat, & Aucan, 2014).

Our proposed technique for estimating virtual tsunami amplitude is applicable not only for tsunami but also for random wavefields of the background ocean infragravity waves. Seismic observations at islands could elucidate ocean infragravity wave activities. The wave action model WAVEWATCH III has recently been extended from the swell band to ocean infragravity waves (Ardhuin et al., 2014) and recovers the observed energy of wave height within 50%. Our method could be used to improve such models.

8 Conclusions

In this study, we consider that an arbitrary tsunami in a flat ocean floor enters a conical island. The scattering wavefield is evaluated using a semi-analytical method, which is an extension of the theory of Fujima and Goto (1994). Then, we calculate ground deformation due to tsunami loading at the center of the conical island using static Green's functions with a first-order correction for bathymetry. In this formulation, the ground motions can be represented by convolution between the transfer functions and the incident tsunami amplitudes at the station. The transfer functions are characterized by a cutoff frequency, f_β, and they approach those given by Ben-Menahem and Singh (2000) for a semi-infinite medium loaded by pressure on the surface without an island. By deconvolving the transfer functions from seismic data, we can infer the incident tsunami wavefield, which can be interpreted as the virtual tsunami amplitude without the island. Thus, we propose a new technique for estimating the virtual tsunami amplitude and propagation direction from seismic data using the assumption of a single plane wave.

First, we apply this technique to seismic records from Aogashima volcanic island when the Torishima Oki earthquake hit on May 2, 2015. The estimated tsunami amplitude is quantitatively consistent with an array observation of pressure gauges close to the island from 1.5 to 20 mHz. The incident angle estimated from the seismic data is also consistent with the ray-theoretical value. We also apply this method to seismic data at four broadband stations located on islands in the Indian ocean for the tsunami earthquake in Mentawai, Indonesia on October 25, 2010. Although the observed frequency range is limited from 0.5 to 2.0 mHz, the incident angles are consistent with ray theoretical values. This method can, therefore, complement offshore tsunami observations.

Because this technique is formulated for an arbitrary incident wavefield, it could be employed not only for tsunami but also for background ocean infragravity waves, which are excited along shorelines by incident ocean swell through nonlinear processes. Further research should develop this method in order to elucidate background ocean infragravity wave activities using broadband seismic stations located on islands.

A Correction of ground deformation for tilt

Following Segall (2010), we estimate the first order correction of displacements $u_i^{(1)}$ $(i = x, y, z)$ for the bathymetry as induced displacement by the first order stress $\sigma_{ij}^{(1)}$ in a cylindrical coordinate (r, θ, z), given by

$$\sigma_{zz}^{(1)} = 0, \tag{A.1}$$

$$\sigma_{rz}^{(1)} = -\frac{dh}{dr}(\sigma_{zz}^{(0)} - \sigma_{rr}^{(0)}), \tag{A.2}$$

$$\sigma_{\theta z}^{(1)} = -\frac{dh}{dr}\sigma_{r\theta}^{(0)} \tag{A.3}$$

at $z = 0$. Here, the 0th-order terms in Cartesian coordinates satisfy

$$\frac{\partial \sigma_{ij}^{(0)}}{\partial x_j} = 0 \tag{A.4}$$

with boundary conditions given by

$$\sigma_{zz}^{(0)} = -p(x, y), \sigma_{zx}^{(0)} = 0, \sigma_{zy}^{(0)} = 0. \tag{A.5}$$

We note the following relationships:

$$\left.\frac{\partial \sigma_{rz}^{(0)}}{\partial z}\right|_{z=0} = \left.\frac{\partial \sigma_{\theta z}^{(0)}}{\partial z}\right|_{z=0} = \left.\frac{\partial \sigma_{zz}^{(0)}}{\partial z}\right|_{z=0} = 0, \tag{A.6}$$

on the free surface of the island. This result is obtained by representing the stress in terms of the Newtonian potential functions (Love, 1929, section 1.1).

The first order displacement can be calculated by convolution between the Green's function in a semi-infinite medium and $\sigma_{ij}^{(1)}$ on the surface. The corresponding components ($\sigma_{rz}^{(1)}$ and $\sigma_{r\theta}^{(1)}$) can be calculated by convolution between $-p$ and static Green's functions of surface traction for normal traction in a semi-infinite space (Jaeger et al., 2007; Segall, 2010). The Green's functions $g_{xx}^{\sigma z}, g_{xy}^{\sigma z}, g_{yy}^{\sigma z}$ in a Cartesian coordinate system are given by

$$g_{xx}^{\sigma z} = \frac{1}{2\pi}\frac{\mu}{\lambda + \mu}\frac{-x^2 + y^2}{r^4} + \frac{1 + 2\nu}{2}\delta(r), \tag{A.7}$$

$$g_{xy}^{\sigma z} = -\frac{1}{2\pi}\frac{\mu}{\lambda + \mu}\frac{2xy}{r^4}, \tag{A.8}$$

$$g_{yy}^{\sigma z} = \frac{1}{2\pi}\frac{\mu}{\lambda + \mu}\frac{x^2 - y^2}{r^4} + \frac{1 + 2\nu}{2}\delta(r). \tag{A.9}$$

Note that Jaeger et al. (2007) does not include two terms of $\delta(r)$ because they are defined outside the source regions. The two terms can be estimated as the limit of a disk load given by Farrell (1972) as r approaches 0, as shown in the next section. For the convolution between $g_{ij}^{\sigma z}$ and $\sigma_{ij}^{(0)}$, calculation in the wavenumber domain is convenient (Segall, 2010). $G_{ij}^{\sigma z}$, which is the Fourier component of $g_{ij}^{\sigma z}$ in the wavenumber domain, is given by

$$G_{xx}^{\sigma z} = \frac{1}{2}\frac{\mu}{\lambda + \mu}\frac{-k_x^2 + k_y^2}{k_x^2 + k_y^2} + \frac{1 + 2\nu}{2} \tag{A.10}$$

$$G_{xy}^{\sigma z} = \frac{1}{2}\frac{\mu}{\lambda + \mu}\frac{-2k_x k_y}{k_x^2 + k_y^2} \tag{A.11}$$

$$G_{yy}^{\sigma z} = \frac{1}{2}\frac{\mu}{\lambda + \mu}\frac{k_x^2 - k_y^2}{k_x^2 + k_y^2} + \frac{1 + 2\nu}{2} \tag{A.12}$$

Figure A.1 shows a typical example of induced 0th-order stress $\sigma_{zz}^{(0)} - \sigma_{rr}^{(0)}$ and $\sigma_{r\theta}^{(0)}$, which is stress induced by the tsunami wavefield with an azimuthal order of 1 ($\zeta_1^{in} = 1$) for Aogashima at 4 mHz. Because $\sigma_{zz}^{(0)} - \sigma_{rr}^{(0)}$ and $\sigma_{r\theta}^{(0)}$ are an order of magnitude smaller than $\sigma_{zz}^{(0)}$ at the surface, we can neglect the first order stress $\sigma_{ij}^{(1)}$. Consequently, the first order displacement $u^{(1)}$ is also negligible. Although the first order correction of normal traction $\sigma_{zz}^{(1)}$ is negligible, those of shear traction, $\sigma_{zx}^{(1)}$ and $\sigma_{zy}^{(1)}$, are significant.

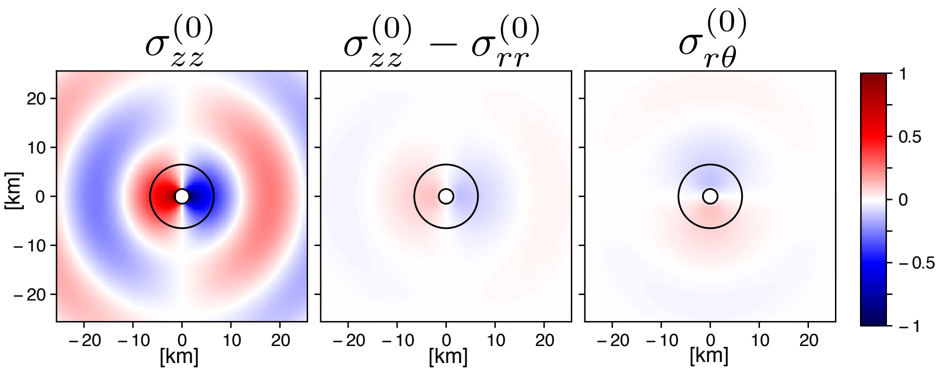

Figure A.1. Stress σ_{zz} is imposed on the surface. σ_{rr} is the induced principle stress on the surface, which is one order of magnitude smaller than the imposed stress. The inner circle shows the radius of the island at sea level, r_0, and the outer circle shows the radius of the island on the seafloor r_1.

B Stress components by surface loads on a half-space

Stress components by surface loads on a half-space are given Jaeger et al. (2007) as

$$\sigma_{xx} = \frac{1}{2\pi}\left[\frac{3x^2 z}{r^5} + \frac{(1-2\nu)(y^2+z^2)}{r^3(z+r)} - \frac{(1-2\nu)z}{r^3} - \frac{(1-2\nu)x^2}{r^2(z+r)^2}\right] \tag{B.1}$$

$$\sigma_{xy} = \frac{1}{2\pi}\left[\frac{3xyz}{r^5} - \frac{(1-2\nu)xy(z+2r)}{r^3(z+r)^2}\right] \tag{B.2}$$

$$\sigma_{yy} = \frac{1}{2\pi}\left[\frac{3y^2 z}{r^5} + \frac{(1-2\nu)(x^2+z^2)}{r^3(z+r)} - \frac{(1-2\nu)z}{r^3} - \frac{(1-2\nu)y^2}{r^2(z+r)^2}\right]. \tag{B.3}$$

Because the surface values are singular, we derive the simplified form on the surface below.

Let us consider that stress components by a disk load (Love, 1929; Lubarda, 2013) are given by

$$\sigma_{rr} = \frac{p}{2}\begin{cases} 1+2\nu, & r<R \\ -(1-2\nu)\frac{R^2}{r^2}, & r \geq R \end{cases} \tag{B.4}$$

$$\sigma_{\theta\theta}, = \frac{p}{2}\begin{cases} 1+2\nu, & r<R \\ (1-2\nu)\frac{R^2}{r^2}, & r \geq R \end{cases} \tag{B.5}$$

where R is the radius of the disk and p is the pressure applied uniformly over the disk area. The limits of stress as R approaches 0 have the following forms:

$$\sigma_{xx} = \frac{1}{2\pi}\frac{\mu}{\lambda+\mu}\frac{-x^2+y^2}{r^4} + \frac{1+2\nu}{2}\delta(r) \tag{B.6}$$

$$\sigma_{xy} = -\frac{1}{2\pi}\frac{\mu}{\lambda+\mu}\frac{2xy}{r^4} \tag{B.7}$$

$$\sigma_{yy} = \frac{1}{2\pi}\frac{\mu}{\lambda+\mu}\frac{x^2-y^2}{r^4} + \frac{1+2\nu}{2}\delta(r). \tag{B.8}$$

These representations are also given by the limit of equation B.1 as z approaches 0.

Acknowledgments

We are grateful to a number of people associated with the IRIS, ORFEUS, and F-net data centers for maintaining the networks and making the data readily available. We would like to acknowledge NOAA Center for Tsunami Research for the tsunami model of 2010 Mentawai earthquake (https://nctr.pmel.noaa.gov/indonesia20101025/). We also thank two anonymous reviewers for many constructive comments. The data analysis was carried out using ObsPy (Krischer et al., 2015). K.N. was supported by JSPS KAKENHI Grant Number JP17H02950, and Y.F. was supported by JSPS KAKENHI Grant Numbers 25247074 and 17K05646. We used data from F-net managed by the National Research Institute for Earth Science and Disaster Prevention (NIED), Japan, IRIS/IDA Seismic Network (https://doi.org/10.7914/SN/II), and GEOSCOPE (https://doi.org/10.18715/GEOSCOPE.G) managed by Institut de Physique du Globe de Paris. Data of ocean bottom pressure gauges used in this study are available from http://p21.jamstec.go.jp.

References

Aki, K., & Richards, P. G. (1980). *Quantitative Seismology* (Vol. 1). W. H. Freeman, San Francisco.

Amante, C., & Eakins, B. W. (2009). *ETOPO1 Global Relief Model converted to PanMap layer format.* PANGAEA. doi: 10.1594/PANGAEA.769615

Ardhuin, F., Gualtieri, L., & Stutzmann, E. (2015). How ocean waves rock the Earth: Two mechanisms explain microseisms with periods 3 to 300 s. *Geophys. Res. Lett.*, *42*(3), 765–772. doi: 10.1002/2014GL062782

Ardhuin, F., Rawat, A., & Aucan, J. (2014, may). A numerical model for free infragravity waves: Definition and validation at regional and global scales. *Ocean Model.*, *77*, 20–32. doi: 10.1016/j.ocemod.2014.02.006

Ben-Menahem, A., & Singh, S. J. (2000). *Seismic Waves and Sources* (2nd ed.). Dover Publications, Incorporated.

Bernard, E. N., & Meinig, C. (2011, sep). History and future of deep-ocean tsunami measurements. In *Ocean. mts/ieee kona* (pp. 1–7). IEEE. doi: 10.23919/OCEANS.2011.6106894

Farrell, W. E. (1972). Deformation of the Earth by surface loads. *Rev. Geophys.*, *10*(3), 761. doi: 10.1029/RG010i003p00761

Fujima, K., & Goto, C. (1994). Characteristics of long waves trapped by conical islands, in japanese. *The Japan Society of Civil Engineers*, *1994*(497), 101-110. doi: 10.2208/jscej.1994.497_101

Fukao, Y., Nishida, K., & Kobayashi, N. (2010). Seafloor topography, ocean infragravity waves, and background Love and Rayleigh waves. *J. Geophys. Res. Solid Earth*, *115*(4), 1–10. doi: 10.1029/2009JB006678

Fukao, Y., Sandanbata, O., Sugioka, H., Ito, A., Shiobara, H., Watada, S., & Satake, K. (2018). Mechanism of the 2015 volcanic tsunami earthquake near Torishima, Japan Mechanism of volcanic tsunami earthquake. *Sci. Adv.*.

Gica, E., Spillane, M., Titov, V., Chamberlin, C., & Newman, J. (2008). *Development of the forecast propagation database for NOAA's Short-Term Inundation Forecast for Tsunamis (SIFT)* (Tech. Rep.).

Gill, A. (1982). *Atmosphere-ocean dynamics.* Elsevier Science.

Jaeger, J., Cook, N., & Zimmerman, R. (2007). *Fundamentals of rock mechanics.* Wiley.

Kanamori, H., Ekström, G., Dziewonski, A., Barker, J. S., & Sipkin, S. A. (1993). Seismic radiation by magma injection: An anomalous seismic event near Tori Shima, Japan. *J. Geophys. Res. Solid Earth*, *98*(B4), 6511–6522. doi: 10.1029/92JB02867

Kânoğlu, U., & Synolakis, C. E. (1998). Long wave runup on piecewise linear topographies. *J. Fluid Mech.*, *374*(November 1998), 1–28. doi: 10.1017/S0022112098002468

Kimura, T., Tanaka, S., & Saito, T. (2013). Ground tilt changes in Japan caused by the 2010 Maule, Chile, earthquake tsunami. *J. Geophys. Res. Solid Earth*, *118*(1), 406–415. doi: 10.1029/2012JB009657

Krischer, L., Megies, T., Barsch, R., Beyreuther, M., Lecocq, T., Caudron, C., & Wassermann, J. (2015). ObsPy: A bridge for seismology into the scientific Python ecosystem. *Comput. Sci. Discov.*, *8*(1). doi: 10.1088/1749-4699/8/1/014003

Lay, T., Ammon, C. J., Kanamori, H., Yamazaki, Y., Cheung, K. F., & Hutko, A. R. (2011). The 25 October 2010 Mentawai tsunami earthquake (M w 7.8) and the tsunami hazard presented by shallow megathrust ruptures. *Geophys. Res. Lett.*, *38*(6), 2–6. doi: 10.1029/2010GL046552

Liu, P. L.-F., Cho, Y.-S., Briggs, M. J., Lu, U. K., & Synolakis, C. E. (1995). Runup of solitary waves on a circular island. *Journal of Fluid Mechanics*, *302*(10), 259–285. doi: 10.1017/S0022112095004095

Longuet-Higgins, M. S. (1967). On the trapping of wave energy round islands. *J. Fluid Mech.*, *29*(04), 781–821. doi: 10.1017/S0022112067001181

Love, A. E. H. (1929). The Stress Produced in a Semi-Infinite Solid by Pressure on Part of the Boundary. *Philos. Trans. R. Soc. A Math. Phys. Eng. Sci.*, *228*(659-669), 377–420. doi: 10.1098/rsta.1929.0009

Lubarda, V. A. (2013). Circular loads on the surface of a half-space: Displacement and stress discontinuities under the load. *Int. J. Solids Struct.*, *50*(1), 1–14. doi: 10.1016/j.ijsolstr.2012.08.029

Moré, J. J., Sorensen, D. C., Hillstrom, K. E., & Garbow, B. S. (1984). *The MINPACK Project, in Sources and Development of Mathematical Software.* Upper Saddle River, NJ, USA: Prentice-Hall, Inc.

Nawa, K., Suda, N., Satake, K., Fujii, Y., Sato, T., Doi, K., … Shibuya, K. (2007). Loading and gravitational effects of the 2004 Indian Ocean tsunami at Syowa Station, Antarctica. *Bull. Seismol. Soc. Am.*, *97*(1A), S271–S278. doi: 10.1785/0120050625

Nishida, K. (2013). Earth's Background Free Oscillations. *Annu. Rev. Earth Planet. Sci.*, *41*(1), 719–740. doi: 10.1146/annurev-earth-050212-124020

Nishida, K. (2017). Ambient seismic wave field. *Proc. Japan Acad. Ser. B*, *93*(7), 423–448. doi: 10.2183/pjab.93.026

Nishida, K., Kawakatsu, H., Fukao, Y., & Obara, K. (2008). Background Love and Rayleigh waves simultaneously generated at the Pacific Ocean floors. *Geophys. Res. Lett.*, *35*(16), L16307. doi: 10.1029/2008GL034753

Okada, Y., Kasahara, K., Hori, S., Obara, K., Sekiguchi, S., Fujiwara, H., & Yamamoto, A. (2004). Recent progress of seismic observation networks in Japan Hi-net, F-net, K-NET and KiK-net. *Earth, Planets Sp.*, *56*(8), xv–xxviii. doi: 10.1186/BF03353076

Radhakrishnan, K., & Hindmarsh, A. C. (1993, dec). *Description and use of LSODE, the Livemore Solver for Ordinary Differential Equations* (Tech.

Rep.). Livermore, CA: Lawrence Livermore National Laboratory (LLNL). doi: 10.2172/15013302
Rawat, A., Ardhuin, F., Ballu, V., Crawford, W., Corela, C., & Aucan, J. (2014, nov). Infragravity waves across the oceans. *Geophys. Res. Lett.*, *41*(22), 7957–7963. doi: 10.1002/2014GL061604
Rawlinson, N. (2005). *FMST: Fast Marching Surface Tomography package Research* (Tech. Rep.). Aust. Natl. Univ.
Rawlinson, N., & Sambridge, M. (2005). The fast marching method: An effective tool for tomographic imaging and tracking multiple phases in complex layered media. *Explor. Geophys.*, *36*(4), 341–350. doi: 10.1071/EG05341
Rhie, J., & Romanowicz, B. (2004, sep). Excitation of Earth's continuous free oscillations by atmosphereoceanseafloor coupling. *Nature*, *431*(7008), 552–556. doi: 10.1038/nature02942
Rodgers, P. W. (1968). The response of the horizontal pendulum seismometer to Rayleigh and Love waves, tilt, and free oscillations of the earth. *Bull. Seismol. Soc. Am.*, *58*(5), 1385–1406.
Sandanbata, O., Watada, S., Satake, K., Fukao, Y., Sugioka, H., Ito, A., & Shiobara, H. (2017). Ray Tracing for Dispersive Tsunamis and Source Amplitude Estimation Based on Green's Law: Application to the 2015 Volcanic Tsunami Earthquake Near Torishima, South of Japan. *Pure Appl. Geophys.*. doi: 10.1007/s00024-017-1746-0
Satake, K. (2015). 4.19 - tsunamis. In G. Schubert (Ed.), *Treatise on geophysics* (Second ed., p. 477 - 504). Oxford: Elsevier. doi: https://doi.org/10.1016/B978-0-444-53802-4.00086-5
Satake, K., Fujii, Y., Harada, T., & Namegaya, Y. (2013). Time and space distribution of coseismic slip of the 2011 Tohoku earthquake as inferred from Tsunami waveform data. *Bull. Seismol. Soc. Am.*, *103*(2 B), 1473–1492. doi: 10.1785/0120120122
Satake, K., & Kanamori, H. (1991). Abnormal tsunamis caused by the June 13, 1984, Torishima, Japan, earthquake. *J. Geophys. Res. Solid Earth*, *96*(B12), 19933–19939. doi: 10.1029/91JB01903
Satake, K., Nishimura, Y., Putra, P. S., Gusman, A. R., Sunendar, H., Fujii, Y., ... Yulianto, E. (2013). Tsunami Source of the 2010 Mentawai, Indonesia Earthquake Inferred from Tsunami Field Survey and Waveform Modeling. *Pure Appl. Geophys.*, *170*(9-10), 1567–1582. doi: 10.1007/s00024-012-0536-y
Segall, P. (2010). *Earthquake and Volcano Deformation*. Princeton University Press.
Smith, R., & Sprinks, T. (1975, nov). Scattering of surface waves by a conical island. *J. Fluid Mech.*, *72*(02), 373. doi: 10.1017/S0022112075003424
Sorrells, G. G., & Goforth, T. T. (1973). Low-Frequency Earth Motion Generated By Slowly Propagating Partially Organized Pressure Fields. *Bull. Seismol. Soc. Am.*, *63*(5), 1583–1601.
Takagi, R., Nishida, K., Maeda, T., & Obara, K. (2018). Ambient seismic noise wavefield in Japan characterized by polarization analysis of Hi-net records. *Geophys. J. Int.*, *215*(3), 1682–1699. doi: 10.1093/gji/ggy334
Tonegawa, T., Fukao, Y., Shiobara, H., Sugioka, H., Ito, A., & Yamashita, M. (2018). Excitation Location and Seasonal Variation of Transoceanic Infragravity Waves Observed at an Absolute Pressure Gauge Array. *J. Geophys. Res. Ocean.*, 40–52. doi: 10.1002/2017JC013488
Vogel, R. M., & Shallcross, A. L. (1996, jun). The moving blocks bootstrap versus parametric time series models. *Water Resour. Res.*, *32*(6), 1875–1882. doi: 10.1029/96WR00928
Wielandt, E., & Forbriger, T. (1999). Near-field seismic displacement and tilt associated with the explosive activity of Stromboli. *Ann. Geophys.*, *42*(3), 407–416. doi: 10.4401/ag-3723
Williams, C. A., & Wadge, G. (2000). An accurate and efficient method for includ-

ing the effects of topography in three-dimensional elastic models of ground deformation with applications to radar interferometry. *J. Geophys. Res.*, *105*(B4), 8103–8120. doi: 10.1029/1999JB900307

Yuan, X., Kind, R., & Pedersen, H. (2005). Seismic monitoring of the Indian Ocean tsunami. *Geophys. Res. Lett.*, *32*(15), L15308. doi: 10.1029/2005GL023464